Electronic Supplementary Material (ESI) for Journal of Materials Chemistry A.

Supporting Information

Electron doping of $Sr_2FeMoO_{6-\delta}$ as high performance anode materials for solid oxide fuel cells

Xin Yang,[abc] Jing Chen,[d] Dhruba Panthi,[c] Bingbing Niu,[a] Libin Lei,[b] Zhihao Yuan,[e] Yanhai Du,[c] Yongfeng Li,[a] Fanglin Chen,[*b] and Tianmin He[*a]

[a]Key Laboratory of Physics and Technology for Advanced Batteries, Ministry of Education, College of Physics, Jilin University, Changchun 130012, PR China
[b]Department of Mechanical Engineering, University of South Carolina, 300 Main Street, Columbia, SC 29208, USA
[c]College of Aeronautics and Engineering, Kent State University, 1400 Lefton Esplanade, Kent, OH 44242, USA
[d]School of Chemistry and Chemical Engineering, Henan University of Technology, Zhengzhou 450001, PR China
[e]School of Materials Science and Engineering, Tianjin University of Technology, Tianjin 300384, PR China

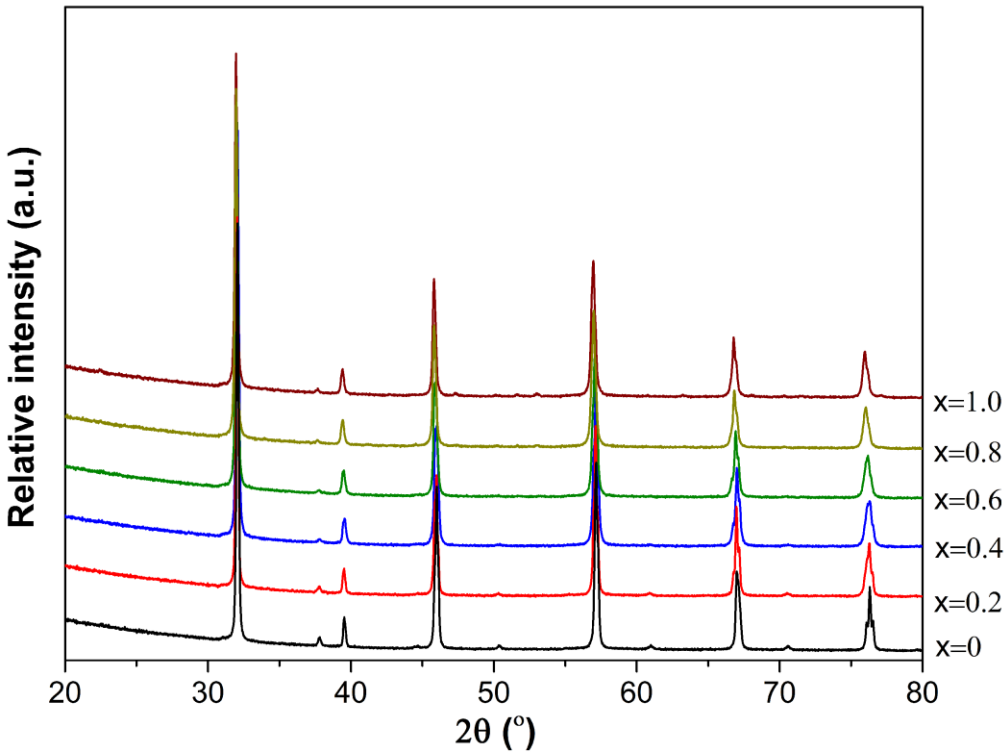

Fig. S1. XRD patterns of the $Sr_{2-x}La_xFeMoO_{6-\delta}$ ($0 \le x \le 1$) powders at room temperature.

* Corresponding author. Email: chenfa@cec.sc.edu (Fanglin Chen)
* Corresponding author. Email: hetm@jlu.edu.cn; hly@mail.jlu.edu.cn (Tianmin He)

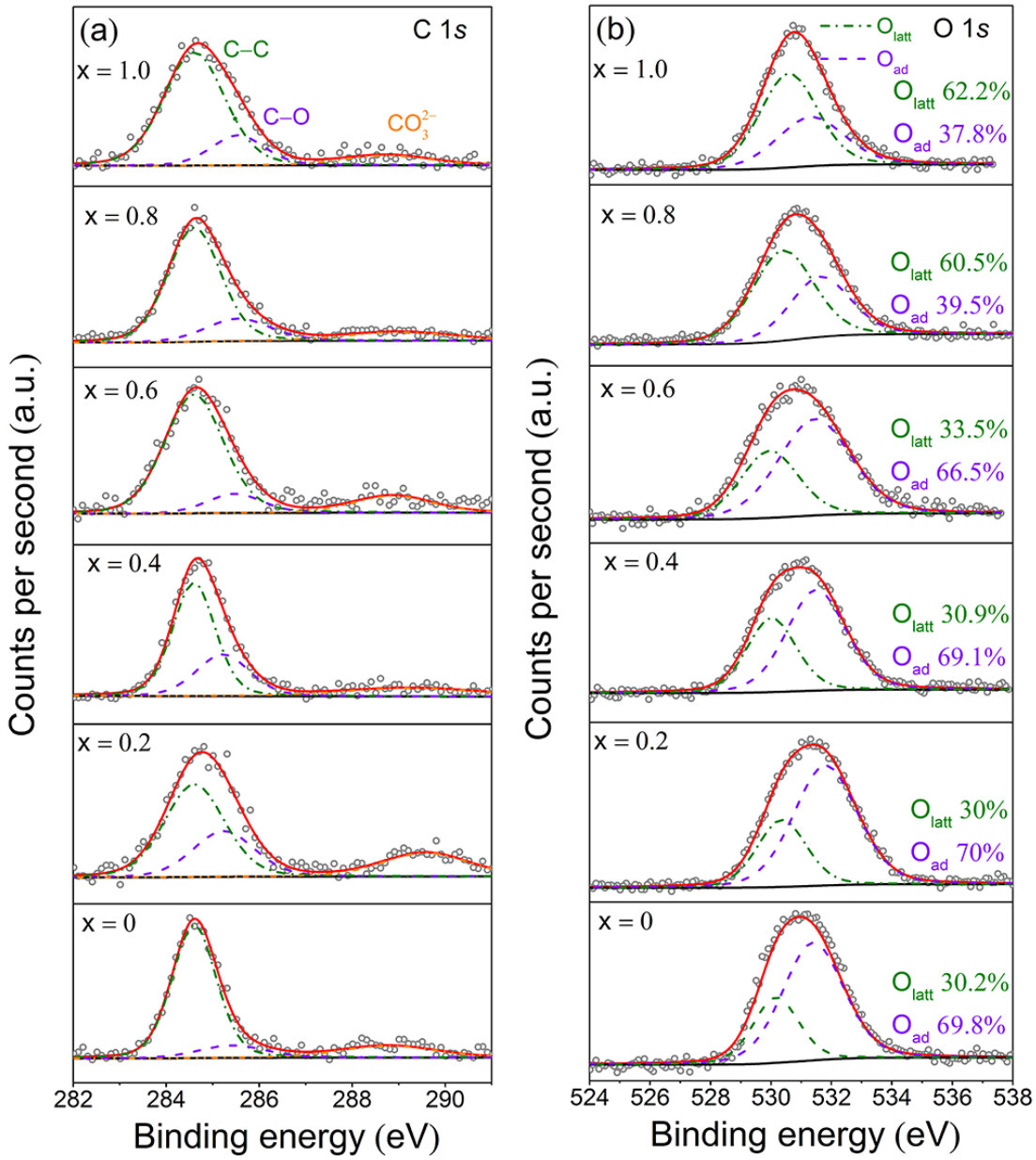

Fig. S2. XPS peak fitting results of (a) C *1s* and (b) O *1s* spectra of $Sr_{2-x}La_xFeMoO_{6-\delta}$($0 \leq x \leq 1$)

The XPS analysis was performed to identify the superfacial cation valences and oxygen species. **Fig. S2(a)** shows the C *1s* core-level spectra. The deconvolution of all XPS spectra

have been calibrated with respect to standard C *1s* peak at 284.6 eV (C–C). The broad O *1s* core-level spectra shown in **Fig. S2(b)** can be deconvoluted and attributed to the lattice oxygen (O_{latt}) and the adsorbed oxygen species (O_{ad}, hydroxyl groups and carbonate compounds). La addition does not seem to affect the O_{ad}/O_{latt} ratio very much within the doping level of $0 \leq x \leq 0.6$ at room temperature, which is a combination of the La doping and the AD contribution, keeping a high level of oxygen-vacancy concentration. In contrast, a significant decrease in O_{ad}/O_{latt} ratio has been observed once the doping level reaches $x = 0.8$. This can be explained by the charge-neutrality requirement, which is the main reason to increase oxygen content so as to compensate the unbalanced charge induced by heterovalent doping.[1]

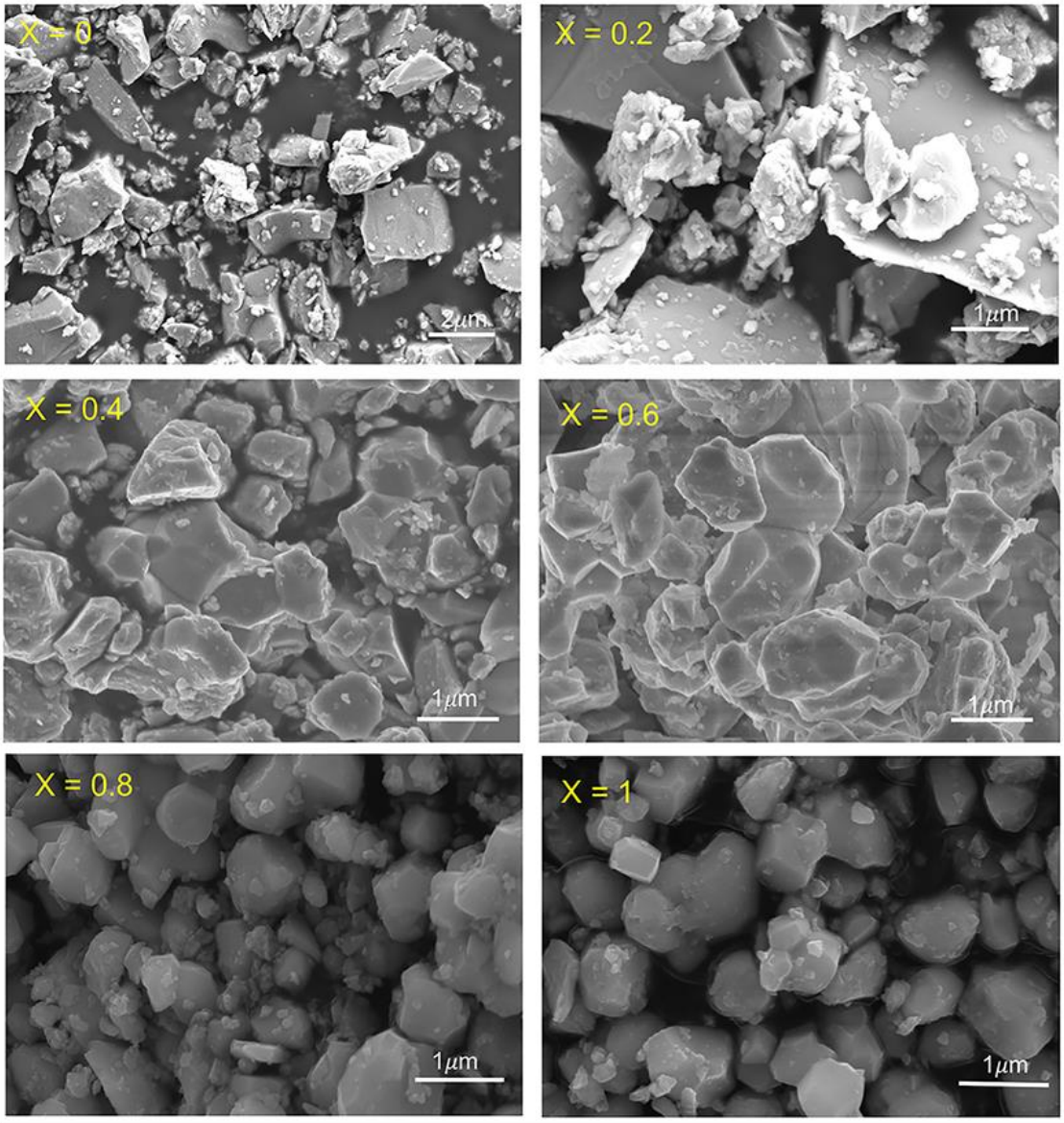

Fig. S3. SEM images of the $Sr_{2-x}La_xFeMoO_{6-\delta}$ powders.

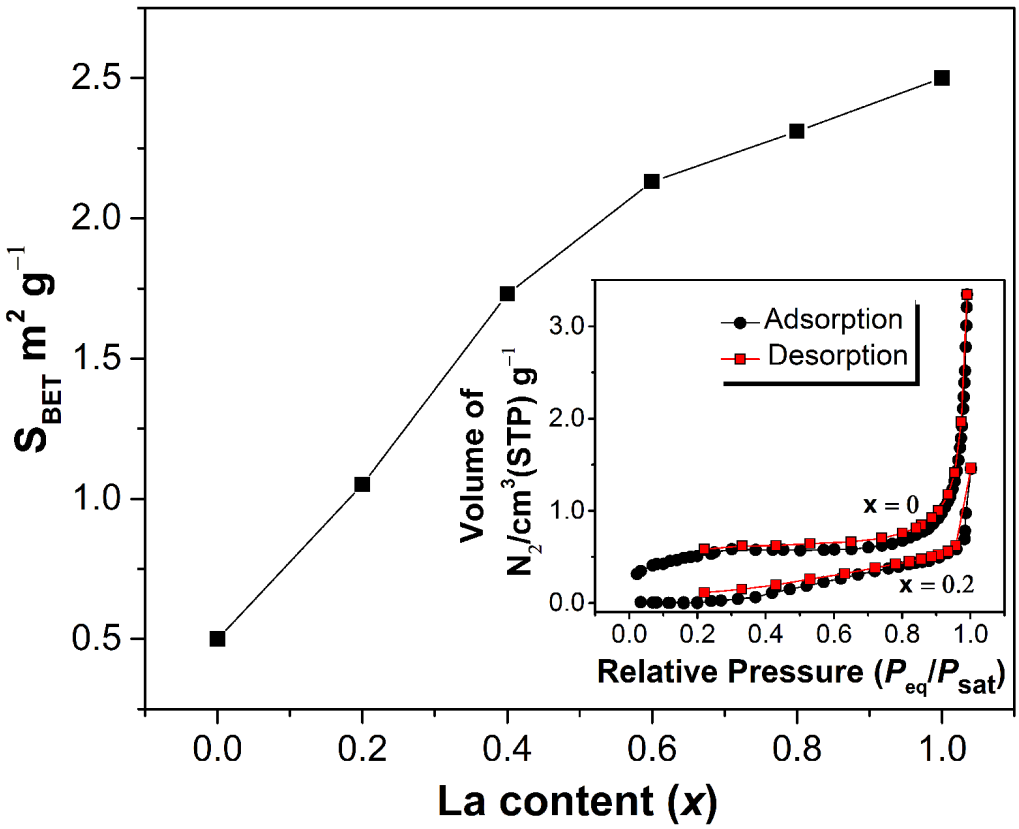

Fig. S4. The BET surface area of the $Sr_{2-x}La_xFeMoO_{6-\delta}$ powders. Inset is the nitrogen sorption-desorption isotherms of the $Sr_{2-x}La_xFeMoO_{6-\delta}(0 \leq x \leq 0.2)$ powders.

The surface area and porosity of $Sr_{2-x}La_xFeMoO_{6-\delta}$ powders were measured with a Micromeritics ASAP 2020 (700VA, 100/115/230 VAC, 50/60 Hz, USA) specific surface area measurement. Brunauer–Emmer–Teller (BET) model was applied in the relative pressure (p_{eq}/p_{sat}) range from 0.01–1. Nitrogen was used as the adsorbate.

The spin-polarized density functional theory (DFT) is employed to characterize the defect nature of La doped $Sr_2FeMoO_{6-\delta}$, including the electronic structure, the AD formation energy ($E_{form}AD$) and the oxygen vacancy formation energy ($E_{form}O^{*}$). In multivalent cations, especially in the mid- to late-first row transition metal oxides, their *d*-orbitals are tightly localized, which usually causes self-interaction error when empoying the pure DFT method.[2] The DFT + U approach, with generalized gradient approximation (GGA) of Perdew–Burke–Ernzerhof (PBE) as the semilocal exchanged-correlation density of functionals, is performed to modify the exchange-correlation density functionals so as to match the experimental results. The $(U–J)_{Fe}$ parameter is set to be 4.0 eV, the average of 3.7 (Fe^{2+}) and 4.3 eV (Fe^{3+}), considering the presence of Fe^{2+} and Fe^{3+} in SLFM2 and SFM. The density of states and the total energy were computed after full geometry optimization. A norm-conserving pseudopotential was constructed. A planewave basis with a cutoff energy of 750 eV and a *k*-point set separation of 0.03/Å was adopted. A 4 × 4 × 4 Monkhorst–Pack *k*-mesh was chosen in creating the 40-atom $Sr_7LaFe_4Mo_4O_{24}$ (x = 0.2) supercell.

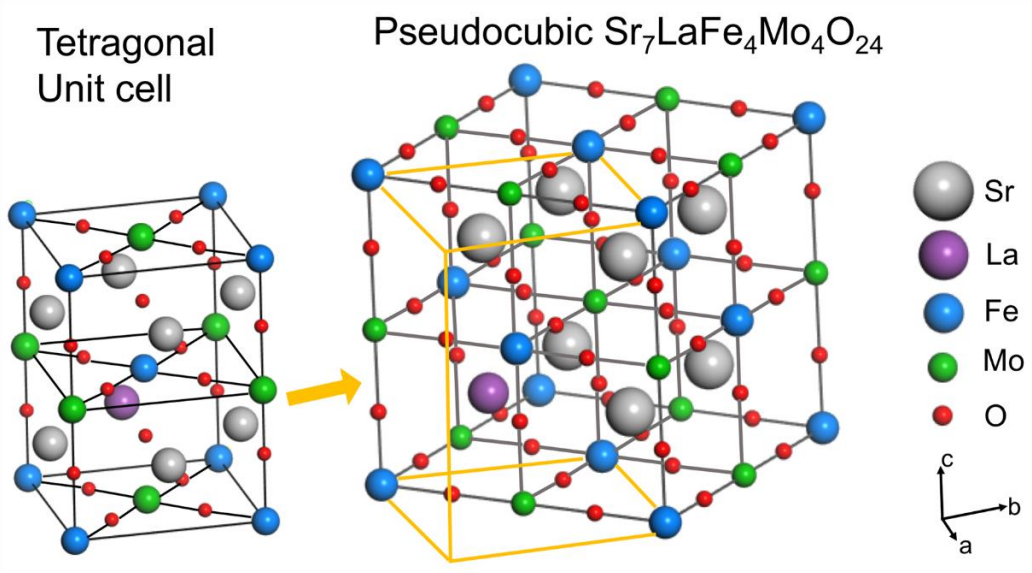

Fig. S5. Correlation of the tetragonal $2Sr_{1.8}La_{0.2}FeMoO_{6-\delta}$ unit cell and the pseudocubic $Sr_7LaFe_4Mo_4O_{24}$ cell.

The initial structural models were created based on the tetragonal unit cells obtained from our Rietveld refinement. As in a tetragonal unit cell, the lattice parameters follow the rule of $\sqrt{2}a = \sqrt{2}b \approx c$. Thus, the lattice parameters in tetragonal unit cell can be related to that of a $\sqrt{2} \times \sqrt{2} \times 1$ pseudocubic supercell, $a_0 = b_0 = \sqrt{2}a \approx c_0$. The pseudocubic supercell with 40-atom was then adopted for calculations because it eliminates the symmetry constrains with the minimum size to stimulate a substitution ratio of $x = 0.2$, an AD concentration above 25 %, and an oxygen vacancy concentration above 4 % ($\delta = 0.25$), which is close to our experimental results. Slightly La substitution in SFM does not change the symmetry, thus, we only show the slightly La substituted SFM supercell. **Supplementary Fig. S5** demonstrates the correlation between the original tetragonal unit cell and the pseudocubic supercell in SLFM supercell. Here we model a $Sr_7LaFe_4Mo_4O_{24}$ supercell by replacing one Sr atom by La to present the case of $Sr_{1.8}La_{0.2}FeMoO_{6-\delta}$. Supercell with exact La content would lead to an extremely large computation (360 atoms).

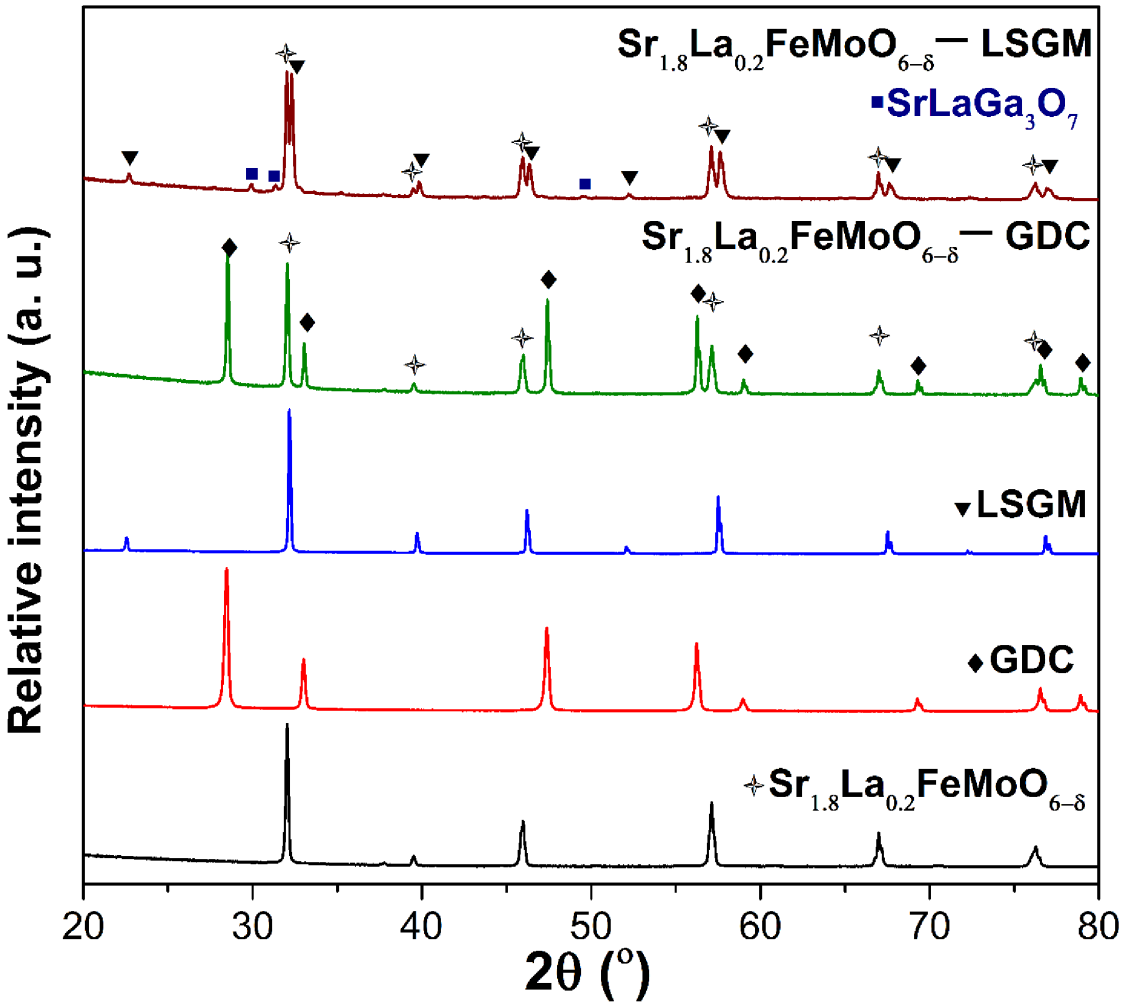

Fig. S6. Chemical compatibility of $Sr_{1.8}La_{0.2}FeMoO_{6-\delta}$ anode with GDC and LSGM electrolytes. XRD patterns of $Sr_{1.8}La_{0.2}FeMoO_{6-\delta}$–LSGM and $Sr_{1.8}La_{0.2}FeMoO_{6-\delta}$ –GDC were obtained on the powder mixture at a mass ratio of 1:1 after calcination in 5% H_2/95% N_2 at 1100 °C for 10 h.

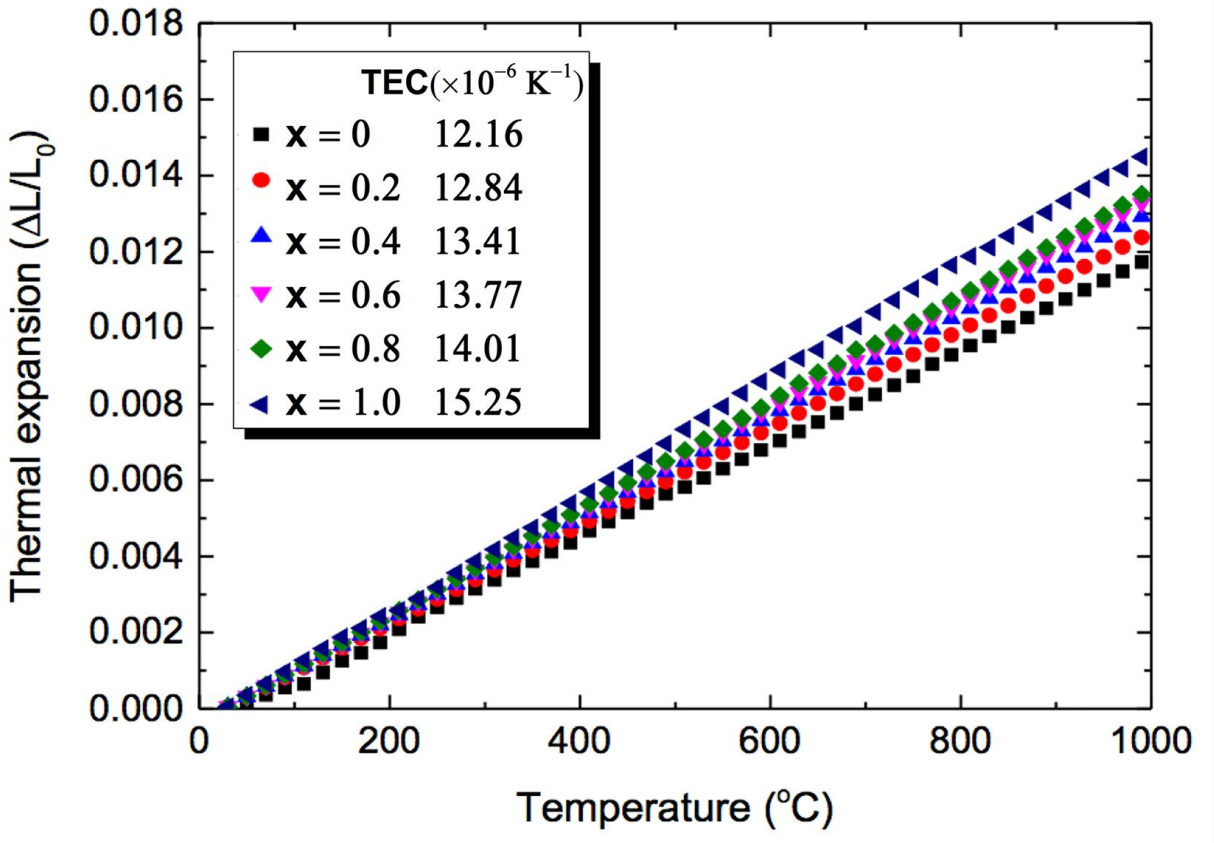

Fig. S7. Thermal expansion curves of $Sr_{2-x}La_xFeMoO_{6-\delta}$ ($0 \leq x \leq 1$) within 30–1000 °C in 5% H_2/95% Ar, with the TEC values shown inside.

The chemical compatibility results based on the SLFM2 suggest that the SLFM series has good compatibility with the GDC electrolyte under the fuel-cell fabrication and operating conditions (**Supplementary Fig. S6**).

The TEC of the SLFM series was obtained using a dilatometer (Netzsch DIL 402C) in 5% H_2/Ar. The testing temperature ranged from 30 °C to 1000 °C at a heating rate of 5 °C min^{-1} under a gas flow rate of 60 mL min^{-1}.

A good thermal expansion matching between an anode and an electrolyte is also important that ensures the good long-term stability. **Supplementary Fig. S7** presents the

thermal expansion curves of the SLFM samples. The TEC values of SLFM ranged from 12.16×10^{-6} K^{-1} to 15.25×10^{-6} K^{-1}. La substitution for Sr led to an increase in TEC values, whereas SLFM2 still maintained a TEC value (12.84×10^{-6} K^{-1}) close to that of the GDC electrolyte (12.5×10^{-6} K^{-1}).

Fuel cells were fabricated based on the chemical compatibility and TEC values between the SLFM anodes and the commonly used electrolytes to achieve high performance and long-term stability. GDC electrolyte was chosen as the buffer layer between the anode and YSZ support to improve the adhesion of the anode on YSZ electrolyte.

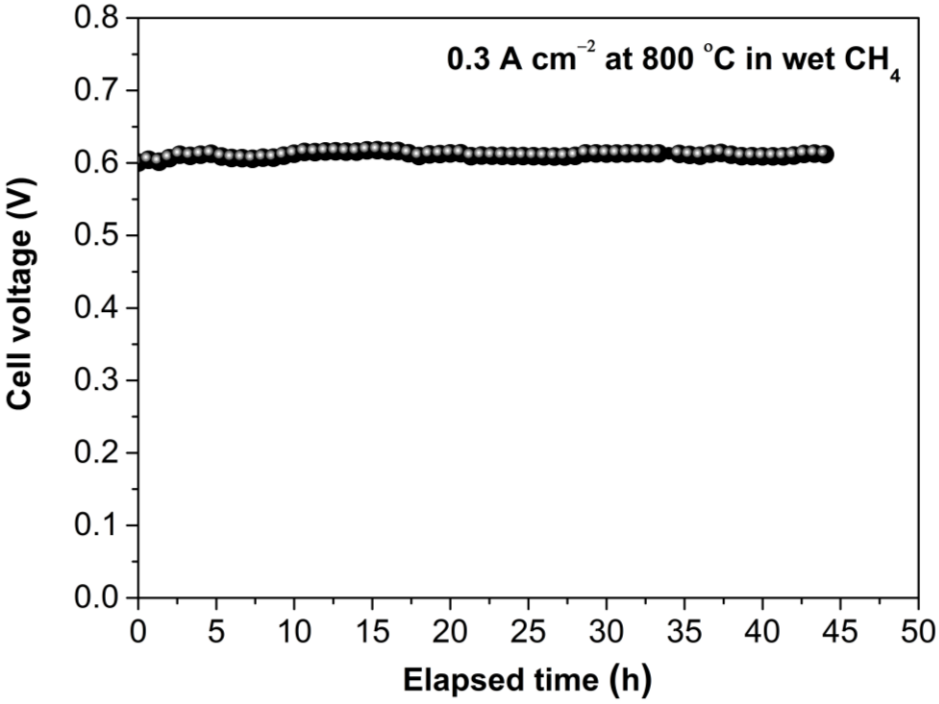

Fig. S8. Short-term stability test of the $Sr_{1.8}La_{0.2}FeMoO_{6-\delta}$ anode under a constant current load of 0.3 A cm^{-2} at 800 °C in CH_4.

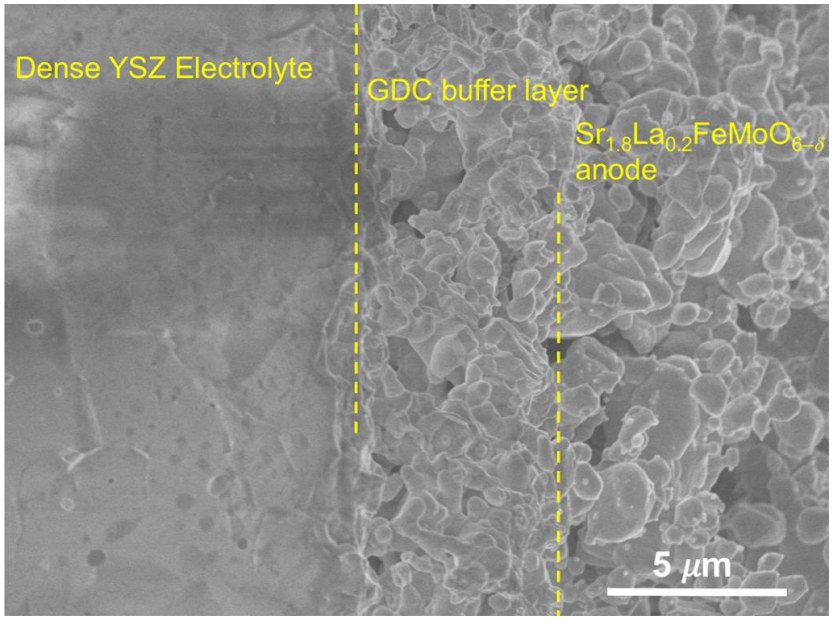

Fig. S9. Cross-sectional SEM image of the spent cell with the $Sr_{1.8}La_{0.2}FeMoO_{6-\delta}$ anode after the short-term stability test in CH_4.

The $E_{form}O^*$ for the perfectly ordered structure was computed from the system total energy by referencing a neutral oxygen atom, as follows:

$$Sr_7LaFe_4Mo_4O_{24} \rightarrow Sr_7LaFe_4Mo_4O_{23} + 1/2E_{O2}\ (g). \qquad (S1)$$

Upon removal of one oxygen atom, the supercell models give an O^* concentration of δ = 0.25. In the perfectly ordered $Sr_7LaFe_4Mo_4O_{23}$ supercell, two different O^* positions need to be considered, including the O^* in the *ab* plane and along the *c* axis, as shown in **Supplementary Fig. S10**.

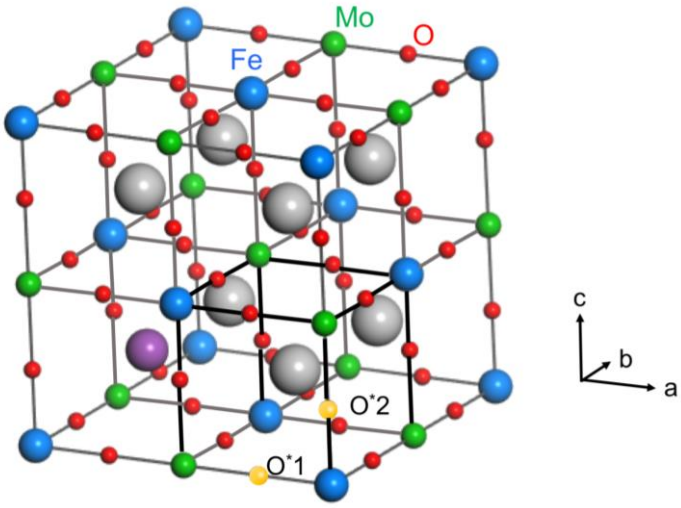

Fig. S10. Oxygen vacancies in the *ab* plane and along the *c* axis in the perfectly ordered $Sr_7LaFe_4Mo_4O_{24}$ structure.

The AD formation energy of the perfect structure can be obtained by computing the system total energy, according to the process:

$Sr_7LaFe_4Mo_4O_{24} \rightarrow$ AD: $Sr_7LaFe_4Mo_4O_{24}$. (S2)

Supplementary Fig. S11 shows all possible AD arrangements in the $Sr_7LaFe_4Mo_4O_{24}$ supercells. The Sr/La atoms are not shown for ease of illustration. The AD formation energy at a certain AD concentration was computed by interchanging the Fe and Mo positions generating different surrounding environments for each anti-site Fe and Mo atoms. According to the Fe and Mo positions, three different relative positions of Fe and Mo have to be considered, including the ADs in the *ab* plane (AD_{ab}), along the diagonal (AD_d), and along the *c* axis (AD_c). Interchanging one pair of Fe–Mo gives an AD degree of 25 %, which is close to our Rietveld refinement results (7.8 % – 32.5 % for x = 0 and 0.2).

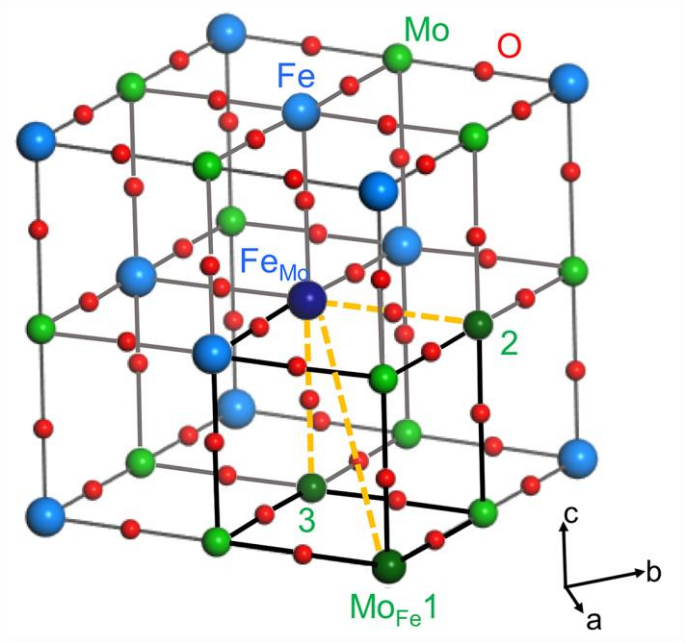

Fig. S11. $Sr_7LaFe_4Mo_4O_{24}$ with anti-site defects along the diagonal, in the *ab* plane, and along the *c* axis of the cube.

Taking the ADs into account, the oxygen vacancy formation energy can be obtained as follows:

AD: $Sr_7LaFe_4Mo_4O_{24} \rightarrow$ AD: $Sr_7LaFe_4Mo_4O_{23} + 1/2E_{O2}$ (g), (S3)

Fig. 7 shows all possible oxygen vacancy arrangements in a $Sr_7LaFe_4Mo_4O_{23}$ supercell with 25 % ADs. As depicted in **Fig. 7a and b**, four different oxygen vacancy positions have to be considered, including the Fe_{Mo}–O^*–Fe in the *ab* plane, the Fe_{Mo}–O^*–Fe along the *c* axis, the Mo_{Fe}–O^*–Mo in the *ab* plane, and the Mo_{Fe}–O^*–Mo along the *c* axis. For the case of AD along the *c* axis depicted in **Fig. 7c**, only two different oxygen vacancy locations have to be considered, including the Fe_{Mo}–O^*–Fe in the *ab* plane and the Mo_{Fe}–O^*–Mo in the *ab* plane.

Reference

[1] M. Retuerto, J. A. Alonso, M. J. Martínez-Lope, N. Menéndez, J. Tornero, M. García-Hernández, *J. Mater. Chem.* **2006**, *16*, 865.

[2] D. D. Sarma, P. Mahadevan, T. Saha-Dasgupta, S. Ray, A. Kumar, *Phys. Rev. Lett.* **2000**, *85*, 2549.

Optimized supercell with lattice vectors and coordinates:

$Sr_7LaFe_4Mo_4O_{24}$ Pseudocubic Cell (total energy = –297.38102 eV)

7.8812999724999999 0.0000000000000000 0.0000000000000000

0.0000000000000000 7.8812999724999999 0.0000000000000000

0.0000000000000000 0.0000000000000000 7.9077000618000000

La 0.2500000000000000 0.2500000000000000 0.2500000000000000

Sr 0.7500000000000000 0.7500000000000000 0.2500000000000000

Sr 0.2500000000000000 0.7500000000000000 0.2500000000000000

Sr 0.7500000000000000 0.2500000000000000 0.2500000000000000

Sr 0.2500000000000000 0.2500000000000000 0.7500000000000000

Sr 0.7500000000000000 0.7500000000000000 0.7500000000000000

Sr 0.2500000000000000 0.7500000000000000 0.7500000000000000

Sr 0.7500000000000000 0.2500000000000000 0.7500000000000000

Fe –0.0004574145466702 –0.0004574145466702 –0.0005509391601448

Fe 0.5004574145466703 0.5004574145466703 –0.0005509391601448

Fe –0.0004574145466702 0.5004574145466703 0.5005509391601448

Fe 0.5004574145466703 –0.0004574145466702 0.5005509391601448

Mo –0.0007437346543252 –0.0007437346543252 0.5008374884210195

Mo 0.5007437346543252 0.5007437346543252 0.5008374884210195

Mo –0.0007437346543252 0.5007437346543252 –0.0008374884210192

Mo 0.5007437346543252 –0.0007437346543252 –0.0008374884210192

O 0.0046980226315546 0.0046980226315546 0.2522511544347887

O 0.4953019773684453 0.4953019773684453 0.2522511544347887

O 0.0010507485148327 0.0010507485148327 0.7475270917987656

O 0.4989492514851672 0.4989492514851672 0.7475270917987656

O 0.0010507485148327 0.4989492514851672 0.7524729082012344

O 0.4989492514851672 0.0010507485148327 0.7524729082012344

O 0.0046980226315546 0.4953019773684453 0.2477488455652113

O 0.4953019773684453 0.0046980226315546 0.2477488455652113

O 0.2519981967789131 0.0044940379695861 0.0044144215449096

O 0.7521949756239654 0.4988876946472384 0.0011400779379020

O 0.2480018032210869 0.4955059620304139 0.0044144215449096

O 0.7478050243760346 0.0011123053527616 0.0011400779379020

O 0.0044940379695861 0.2519981967789131 0.0044144215449096

O 0.4988876946472384 0.7521949756239654 0.0011400779379020

O 0.0011123053527616 0.7478050243760346 0.0011400779379020

O 0.4955059620304139 0.2480018032210869 0.0044144215449096

O 0.2519981967789131 0.4955059620304139 0.4955855784550904

O 0.7521949756239654 0.0011123053527616 0.4988599220620980

O 0.2480018032210869 0.0044940379695861 0.4955855784550904

O 0.7478050243760346 0.4988876946472384 0.4988599220620980

O 0.0011123053527616 0.7521949756239654 0.4988599220620980

O 0.4955059620304139 0.2519981967789131 0.4955855784550904

O 0.0044940379695861 0.2480018032210869 0.4955855784550904

O 0.4988876946472384 0.7478050243760346 0.4988599220620980